Composites: Part A 181 (2024) 108139

Contents lists available at ScienceDirect

Composites Part A

journal homepage: www.elsevier.com/locate/compositesa

A simple stress-based failure criterion for predicting unfolding failure

S. Bushpalli [a,b,*], P. Zumaquero [b], B. López-Romano [a], E. Graciani [b]

[a] FIDAMC, Foundation for the Research, Development and Application of Composite Materials, Avda. Rita Levi Montalcini 29, 28906 Getafe, Madrid, Spain
[b] Grupo de Elasticidad y Resistencia de Materiales, Escuela Técnica Superior de Ingeniería, Universidad de Sevilla, Spain

ARTICLE INFO

Keywords:
Delamination
Mechanical properties
Strength
Unfolding failure

ABSTRACT

Corners of highly curved composite laminates experience unfolding failure when they are loaded under opening bending moments. This work provides a comprehensive experimental test campaign and a detailed stress analysis to gain insight into the different failure mechanisms occurring in curved CFRP laminates made from three different thermoset materials. Two distinct failure mechanisms are observed: firstly, traditional unfolding failure, occurring in unidirectional curved composite laminates exhibiting pure interlaminar delamination associated to the maximum interlaminar stresses in the curved region and, secondly, induced unfolding failure occurring in multi-directional curved composite laminates, where the failure is assumed to be originated from intralaminar matrix cracks which, under the presence of high interlaminar stresses, further propagate as an interlaminar delamination. A simple stress-based failure criterion is proposed to predict the unfolding failure load which provides a fairly good agreement with the experimental results in all cases.

1. Introduction

In recent years, the application of composite materials in complex engineering structures under various loading conditions has seen a significant increase, driven by their exceptional mechanical properties and lightweight nature. However, as these materials find their way into critical components, understanding their failure mechanisms becomes paramount. In particular, the curved zones of complex structures, such as L-joints, T-joints, and other highly curved configurations, typically constitute one of the weakest parts of the component, thus demanding a detailed investigation of the failure behavior.

Failure of curved laminates has been extensively studied by various authors in [1–13]. Among them, [1–5] were the first ones to highlight the matrix induced delamination in curved laminates [1–3], T-joints [4] and Ω-specimens [5]. The use of stress-based failure criteria based on interlaminar stresses [6] or in a combination of interlaminar and intralaminar stresses [7] showed a thickness dependence on the interlaminar tensile strength in curved laminates which has been extensively studied both numerically and experimentally [8–13].

The present study deals with the failure mechanisms in highly curved composite laminates under opening bending moments, examining two distinct failure scenarios, as introduced in [14]: traditional unfolding failure, observed in unidirectional (UD) curved laminates, and induced unfolding, prevalent in non-UD curved laminates. In traditional unfolding, the final failure is associated with delamination caused by interlaminar stresses, while, conversely, induced unfolding is characterized by failure initiation through intralaminar failure, which, under the presence of sufficiently high interlaminar stresses, subsequently propagates as a delamination, ultimately leading to the final failure of the laminate.

The analysis of the stress states and failure locations in several sets of coupons of curved composite laminates carried out in [14], led to the conclusion that unfolding failure took place immediately after the onset of the first intralaminar damage. In the present work, several different sets of coupons of curved composite laminates have been selected to emphasize that in multidirectional laminates, unfolding failure is initiated by an intralaminar damage. Notwithstanding, it is important to note that the failure of the sample doesńt always happen immediately after the first intralaminar damage onset. Depending on the material properties and the stacking sequences, a significant increase in the applied load might be necessary to cause the intralaminar damage to unstably propagate as a delamination, ultimately leading to failure of the sample.

The objective of the current work is to introduce a simple stress-based failure criterion for predicting the unfolding failure load by considering three possible failure mechanisms, for which the failure moment predictions are analytically calculated utilizing the stress analysis tool developed in [15] which enable us to determine the stress

* Corresponding author at: Grupo de Elasticidad y Resistencia de Materiales, Escuela Técnica Superior de Ingeniería, Universidad de Sevilla, Spain.
E-mail address: sinbus@alum.us.es (S. Bushpalli).

https://doi.org/10.1016/j.compositesa.2024.108139
Received 30 August 2023; Received in revised form 7 March 2024; Accepted 9 March 2024
Available online 11 March 2024

states in the critical failure-prone regions of the curved laminates. The analytical model evaluates the three-dimensional field of strains and stresses in a singly curved laminate loaded in bending and under a homogeneous change of temperature, following the hypothesis of Spencer et al. [16] according to which the stresses and strains depend only on the radial coordinate (that is, sufficiently far away from free-edges and changes of curvature). This simple stress-based failure criterion, in combination with the stress analysis tool, can be easily implemented in any programming language in order to be used in the design stage of the composite components, allowing us to determine the unfolding load of curved components with multidirectional stacking sequences in a short period of time.

To show the accuracy of the proposed criterion, an extensive test campaign on three different thermoset materials is presented in which the experimental results are successfully compared with the analytical predictions. Additionally, the delamination locations of the tested samples are compared with the stress analysis results to assess the efficiency of the proposed failure criterion.

2. Test campaign

This section provides a comprehensive overview of the materials and methods employed in the unfolding failure study. Firstly, three different thermoset materials employed in the study are described. Secondly, the stacking sequences considered, with some of them specifically optimized to accentuate the induced unfolding phenomenon, are presented. Finally, the last subsection describes the procedures used to evaluate the Curved Beam Strength (*CBS*) of each coupon and the Interlaminar Tensile Strength (ILTS) of the materials under investigation.

2.1. Materials and manufacturing processes

The present investigation of the unfolding failure involves three different carbon-fiber reinforced thermoset polymer-matrix materials, designated as M1, M2 and M3. Each of these materials possesses unique stiffness properties and interlaminar and intralaminar strengths.

Material denoted as M1 consists of AS4/8552, which is an intermediate modulus composite material that comprises of AS4 carbon fibers and 8552 epoxy resin matrices. For stress calculation in material M1 samples, the following stiffness properties were considered [17]: $E_{11} = 132$ GPa, $E_{22} = E_{33} = 9.23$ GPa, $\nu_{12} = \nu_{13} = 0.302$, $\nu_{23} = 0.4$, $G_{12} = G_{13} = 4.82$ GPa and $G_{23} = E_{22}/(2+2\nu_{23})$, where subindexes 1, 2 and 3 respectively refer to the fiber direction, the in-plane direction perpendicular to the fiber and the thickness direction. To evaluate residual stresses, the stress-free temperature has been considered equal to the curing temperature, being 155 K above room temperature, along with the following thermal expansion coefficients [18]: $\alpha_1 = 0.70$ με/K, $\alpha_2 = 36.3$ με/K and $\alpha_3 = 60$ με/K. Notice that, following the results presented in [18], it has been considered that $\alpha_3 \neq \alpha_2$. Notwithstanding since the plies are free to deform in the thickness direction, the value of α_3 does not affect the calculation of residual stresses and the same results would have been obtained with the classical hypothesis $\alpha_3 = \alpha_2$. This hypothesis has been considered in materials M2 and M3 due to the lack of information about the actual value of α_3.

Materials M2 and M3 consist of high strength and stiffness carbon fibers with epoxy resin matrices employed in commercial aircraft structures. Due to confidentiality reasons, the specific details of these materials, including their names and proprietary information are undisclosed.

For materials M1 and M3, a comprehensive experimental test campaign, involving fabrication, testing and post-processing of the results, has been carried out. Conversely, the tests of material M2 are the same used in [14]. However, as will be detailed later, test results have been re-analyzed, following the same procedures employed with materials M1 and M3, to include some aspects that were neglected or assumed in [14].

Table 1
Unidirectional layups and test configurations (all dimensions are in mm).

Set	w	l_t	l_b	r_i	D	Layup
M1.UD.08	30	20	36	5	10	$[0_8]$
M1.UD.16	30	22	40	5	10	$[0_{16}]$
M1.UD.24	30	25	44	5	10	$[0_{24}]$
M1.UD.32	40	34	55	5	20	$[0_{32}]$
M3.UD.06	30	20	36	3	10	$[0_6]$
M3.UD.16	30	20	40	3	10	$[0_{16}]$
M3.UD.24	30	26	50	5	10	$[0_{24}]$
M3.UD.32	40	36	60	5	20	$[0_{32}]$
M3.UD.48	50	40	68	5	20	$[0_{48}]$

In general, unidirectional prepregs with a nominal thickness of 0.184 mm are used to manufacture curved panels, from which individual coupons are later cut to required dimensions, adhering to specified test standards referenced in [19,20]. The fabrication procedures for each material were carried out in different facilities and thus differ in several aspects. The fabrication of M1 panels (manufactured and tested at the University of Seville) involved manual laying of plies onto a steel tool set at a 90° angle, with the desired corner radius (this radius forms the inner radius of the curved region). To ensure quality, heat from an air heating device, pressure using a spatula and a periodic vacuum compaction (every fifth layer) are applied to avoid any void formation. The curved panels are then subjected to the curing process and subsequently cut to the desired dimensions [21]. For M3 specimens (manufactured and tested at FIDAMC), the process begins with the automated tape layup technique, where flat panels are initially manufactured. These panels are then placed on a tool with 90° angle and a desired corner radius and are further subjected to hot forming process to achieve the intended shape. Following hot forming, the panels, along with the tools, undergo a curing procedure in an autoclave at the designated temperature and time. After curing, the curved panels are detached from the tool to undergo ultrasonic Non-Destructive Testing (NDT) for quality assurance. Once approved through NDT, the specimens are cut according to the required dimensions. The manufacturing process of M2 panels, (manufactured and tested by third parties), remains undisclosed due to confidentiality reasons.

Notice that, as stated in [21], manufacturing of highly curved composite panels induces a certain level of misalignment in the fibers oriented at 0°. These misalignments have not been considered in the stress analysis carried out in the present study.

2.2. Stacking sequences

Test samples analyzed in the present study can be divided into four different groups:

- Group UD consist of samples with $[0_n]$ stacking sequences, (with 0° being the direction following the curvature of the samples).
- Group CP consist of samples with $[0, 90_2, 0_n]_S$ stacking sequences. These stacking sequences are expected to exhibit early intralaminar damage in the 90° layers located in the inner radii.
- Group QI consists of samples with quasi-isotropic stacking sequences. These stacking sequences have been selected for being, among all quasi-isotropic stacking sequences, those prone to experience early intralaminar damage in the 90° layers located in the inner radii [22].
- Group MD consists of multidirectional stacking sequences, some of which are actually employed in commercial aircraft structures following spar/rib configurations.

To reference the coupons used in the study, a naming convention has been established according to which all samples are named as Mi.SS.NLj-k, where Mi (M1, M2, M3) denotes the material type, SS (UD,CP,QI,MD) refers to each of the stacking sequences and/or test set-ups of the

Table 2
Non-UD layups and test configurations (all dimensions are in mm).

Set	w	l_t	l_b	r_i	D	Layup
M1.CP.08	30	20	36	5	10	$[0, 90_2, 0]_S$
M1.CP.16	30	22	40	5	10	$[0, 90_2, 0_5]_S$
M1.CP.24	30	25	44	5	10	$[0, 90_2, 0_9]_S$
M1.CP.32	40	35	55	5	20	$[0, 90_2, 0_{13}]_S$
M1.QI.08	30	20	35	5	10	$[45, -45, 90, 0]_S$
M1.QI.16	30	22	40	5	10	$[45, -45, 90_2, 0, 45, -45, 0]_S$
M1.QI.24	30	25	44	5	10	$[45, -45, 90_2, 45, -45, 90, 0_2, 45, -45, 0]_S$
M1.QI.32	40	35	56	5	20	$[(45, -45, 90_2)_2, (0, 45, -45, 0)_2]_S$
M2.MD.09	25	20	35	3.34	10	$[45, -45, 90, 45, 0, -45, 90, -45, 45]$
M2.MD.16a	25	26	40	5.06	15	$[45, -45, 90, -45, 45, 0, 45, -45]_S$
M2.MD.16b	50	26	40	5.06	15	$[45, -45, 90, -45, 45, 0, 45, -45]_S$
M2.MD.28	40	30	47	6.85	15	$[45, -45, 90_2, -45, 45, 0, (45, -45)_2, 0, 45, -45]_S$
M2.MD.48a	40	43	69	11.2	15	$[(45, 0\text{-}45, 90)_6]_S$
M2.MD.48b	40	43	69	11.2	15	$[45, -45, 90_3, -45, 45, 0_2, (45, -45)_2, 0, (45, -45)_{10}]_S$
M3.CP.08	30	20	36	5	10	$[0, 90_2, 0]_S$
M3.CP.16	30	22	40	5	10	$[0, 90_2, 0_5]_S$
M3.CP.24	30	26	50	5	10	$[0, 90_2, 0_9]_S$
M3.CP.32	40	36	60	5	20	$[0, 90_2, 0_{13}]_S$
M3.CP.48	50	40	68	5	20	$[0, 90_2, 0_{21}]_S$
M3.MD.10	30	22	38	5	10	$[45, 90, -45, 0, 45, -45, 0, -45, 90, 45]$
M3.MD.12	30	22	38	5	10	$[45, -45, 90, -45, 45, 0_2, 45, -45, 90, -45, 45]$
M3.MD.16a	30	24	40	5	10	$[45, -45, 90, -45, 45, 0, 45, -45]_S$
M3.MD.16b	30	24	40	5	10	$[45, 90, -45, -45, 45, 0, 45, -45]_S$
M3.MD.28a	40	30	50	6	10	$[45, -45, 90_2, -45, 45, 0, (45, -45)_2, 0, -45, 45]_S$
M3.MD.28b	30	22	38	10	20	$[45, -45, 90_2, -45, 45, 0, (45, -45)_2, 0, -45, 45]_S$
M3.MD.28c	40	30	50	6	10	$[45, 90, -45, 90, -45, 45, 0, (45, -45)_2, 0, -45, 45]_S$
M3.MD.28d	30	22	38	10	20	$[45, 90, -45, 90, -45, 45, 0, (45, -45)_2, 0, -45, 45]_S$
M3.MD.36a	40	42	66	6	20	$[45, -45, 90_2, (-45, 45)_2, 0, (45, -45)_2, 0, (-45, 45)_2]_S$
M3.MD.36b	40	42	66	6	20	$[45, 90, -45, 90, (-45, 45)_2, 0, (45, -45)_2, 0, (-45, 45)_2]_S$

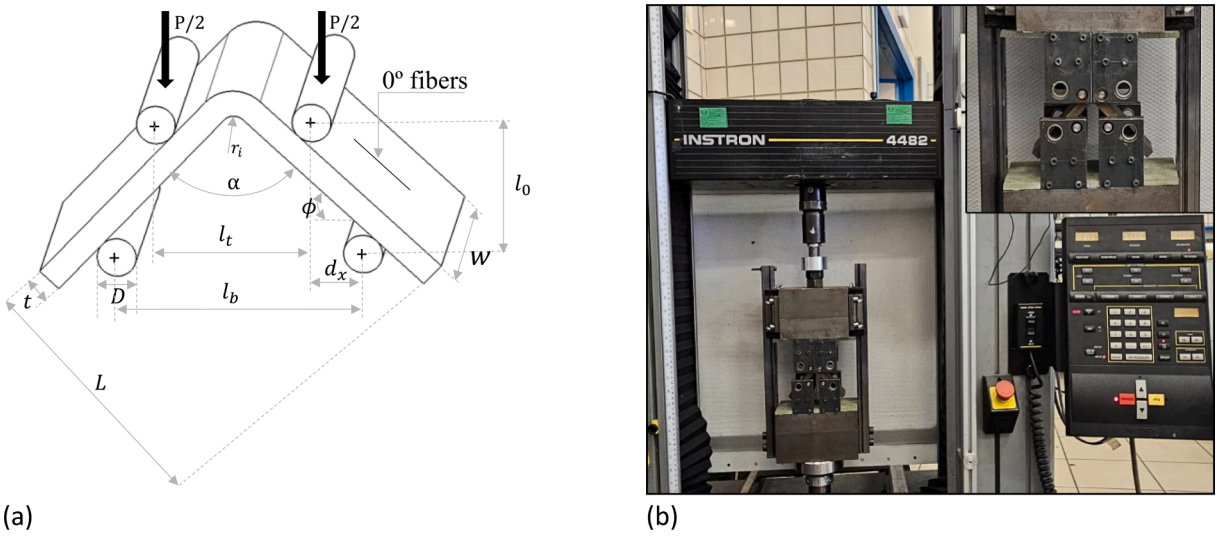

Fig. 1. Four-point bending test: (a) Test specifications and loading parameters, (b) Test device at the University of Seville.

aforementioned groups of samples defined in Tables 1 and 2, NLj refers to the number of layers and k (1, 2,…) identifies the individual coupons in each set. The number of layers, NLj, is expressed with two digits. When multiple test configurations of the same material and group, all having the same number of layers, they are distinguished using lower-case letters (28a, 28b,…). For instance, the notation M2.MD.10-5 refers to the fifth coupon of a multidirectional-layup set of samples with a layup of ten layers (see Table 2) made of material M2.

2.3. Test data reduction

For the sets of samples whose dimensions are listed in Tables 1 and 2, the load/deflection curves of the L-shaped samples, loaded in bending with the aid of a four-point bending test device, see Fig. 1, have been experimentally recorded, see Appendix B. The tests have been carried out according to the procedures described in AITM1-0069 standard [19] (used to define sample dimensions and test configurations) and ASTM D 6415/D 6415 M standard [20] (used to define test conditions and for results postprocessing). Applied load and crosshead displacement is read from the calibrated universal testing machine. Crosshead speed is set to 2 mm/min. To avoid the introduction of frictional forces, ball bearings are employed in the load and support rollers. No additional instrumentation for detecting damage, apart from the post-mortem sample inspection described later is used during the test. Notice that, since one

Table 3
Average *CBS* and *ILTS* of the material M1 sets of samples.

Set	F_{max} [kN]	$U(F_{max})$ [mm]	*CBS* [N·mm/mm]	*ILTS* [MPa]
M1.UD.08	1.37 ± 0.19	5.79 ± 0.27	459 ± 54	81.0 ± 8.5
M1.UD.16	2.76 ± 0.16	3.93 ± 0.18	1260 ± 58	102.8 ± 4.7
M1.UD.24	4.84 ± 0.42	4.03 ± 0.28	2440 ± 150	118.8 ± 7.5
M1.UD.32	5.28 ± 0.65	3.16 ± 0.41	3420 ± 490	114 ± 16
M1.CP.08	0.49 ± 0.07	4.06 ± 0.61	194 ± 18	–
M1.CP.16	1.00 ± 0.15	2.44 ± 0.38	525 ± 66	–
M1.CP.24	2.16 ± 0.38	2.45 ± 0.35	1250 ± 190	–
M1.CP.32	2.99 ± 0.39	2.40 ± 0.14	1970 ± 230	–
M1.QI.08	0.529 ± 0.088	6.24 ± 0.55	160 ± 18	–
M1.QI.16	1.164 ± 0.050	4.78 ± 0.13	512 ± 16	–
M1.QI.24	1.91 ± 0.12	4.05 ± 0.18	990 ± 51	–
M1.QI.32	2.37 ± 0.17	3.98 ± 0.24	1465 ± 96	–

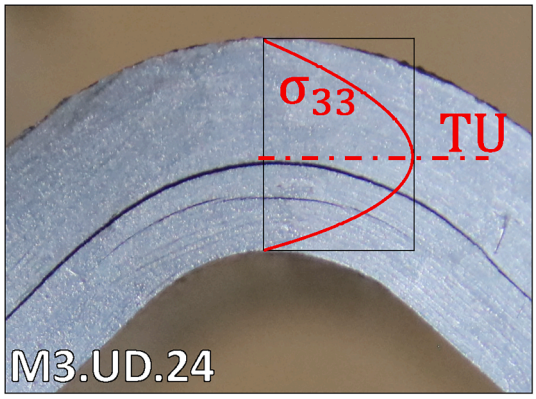

Fig. 2. Correlation between stress solution and failure locations in a typical M3.UD.24 sample at failure.

of the objectives of the test campaign is to use actual test configurations used in industry, in some cases, sample dimensions or loading parameter are not in agreement with the requirements established in the test standards. Despite this fact, the procedures described in the ASTM [20] standard have been employed to determine the Curved Beam Strength, *CBS*, of each coupon, defined as:

$$CBS = \frac{M_{exp}}{w} \tag{1}$$

where M_{exp} is the moment applied in the curved section when failure of the sample takes place and w is the width of the sample. Experimental failure moment M_{exp} can be determined from the experimental failure load and corresponding displacement measurements using equations (1)-(3) in [20], considering the dimensions of the test configuration provided in Tables 1 and 2 and the sample dimensions. The individual dimensions of each sample, not reported for the lack of space, are employed in the calculation of the *CBS*.

In Table 3, the average values (along with the 95 % confidence interval determined from the set of individual measurements [23]) of failure force and displacement for the UD, CP, and QI samples made of material M1 are displayed, along with their respective *CBS* calculations. The same procedure was adopted to obtain the results in samples made of materials M2 and M3. However, to preserve confidentiality, the results for materials M2 and M3 will be presented in a non-dimensional manner in the subsequent sections.

For each material, the Interlaminar Tensile Strength, S_{33}, is determined based on the *CBS* of the $[0_n]$ samples that were tested. The calculation involves finding the maximum of the σ_{33} interlaminar stress, using equations (4)-(6) in [20]. As can be seen in Fig. 2, where the interlaminar stress solution is shown superimposed onto a post-mortem image of a tested sample, predicted failure location is in excellent agreement with the main crack appearing in the sample.

The ILTS for material M1, has been obtained using the UD sets shown in Table 3, while considering the dimensions of the test configuration provided in Table 1 along with the material M1 stiffness properties, resulting in an average value of $(S_{33})_{M1} = 103.5 \pm 8.8$ MPa. This value is slightly different to the ILTS value reported in [21], since a different set of samples has been considered to obtain the average value. Notice that the sample dimensions employed for determining $(S_{33})_{M1}$ are not in agreement with the requirements established in ASTM D 6415/D 6415 M standard. Notwithstanding, the reported value of $(S_{33})_{M1}$ is considered a good approximation of the actual ILTS of the material.

The ILTS values for materials M2, $(S_{33})_{M2} = 60$ MPa, and M3, $(S_{33})_{M3} = 87.5$ MPa, have been obtained following the same procedure described for material M1, although details on the actual calculations are concealed due to confidentiality reasons. Results of the tested UD samples of materials M1 and M3 are respectively shown in Fig. 3(a)–(b), where the average values of each set of samples is indicated with a square, and the individual results of each sample are also reported. For material M3, samples with two distinct inner radii, r_i, have been tested. Although only the samples with $r_i = 5$ mm have been used to determine the ILTS of material M3, all results are presented in Fig. 3(b) to show the range of variability in the results.

Notice that, considering all UD test results of materials M1 and M3 presented in Fig. 3, a range of $0.78 \leq \sigma_{33,max}/S_{33} \leq 1.15$ is obtained. This high variability of the results is inherent to the test of L-shaped samples, especially in thin samples and samples with small inner radius, possibly due to the difficulty in obtaining a good alignment and compaction in the corner during manufacturing.

The in-plane strength of the material in the direction perpendicular to the fibers, denoted as S_{22}, is taken from existing literature or previous test campaigns carried out. For material M1 $(S_{22})_{M1} = 64$ MPa is taken

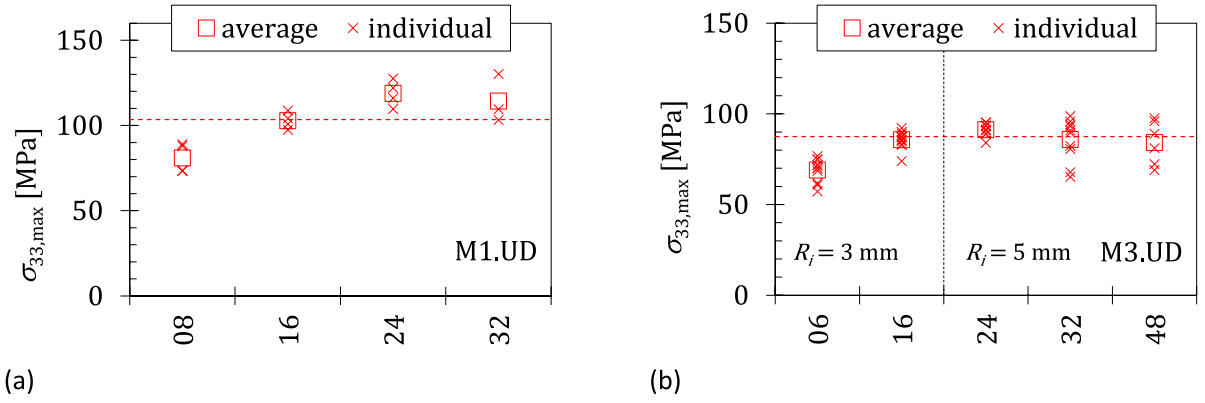

Fig. 3. Test results of UD samples: (a) material M1, (b) material M3.

from [17], for material M3 $(S_{22})_{M2} = 50$ MPa is obtained and for material M2 $(S_{22})_{M2} = 97$ MPa.

3. Stress analysis and failure criteria

In order to analyze the failure mechanisms associated with the unfolding failure based on stress states associated with the failure loads, let us consider the following reference system where the ply stresses in the orthotropic directions are denominated as σ_{11}, which represents the normal stresses along the fiber direction (with 0° fibers following the curvature and into the straight arms), σ_{22}, which represents the normal stresses in the in-plane direction perpendicular to the fiber and σ_{33}, which represents the normal stresses in the direction of the thickness of the laminate, commonly referred to as interlaminar normal stress (INS).

As mentioned previously, the failure behavior of UD curved laminates follows a conventional mode, where the final breakdown of the composite laminate occurs due to delamination induced by σ_{33} interlaminar stresses. When σ_{33} reaches the interlaminar strength of the material, i.e., when $\sigma_{33} = S_{33}$, delamination is initiated at the location in which the maximum σ_{33} is achieved. This delamination progresses unstably, immediately leading to the final failure of the laminate.

Conversely, non-UD curved laminates exhibit a distinct failure mechanism, known as induced unfolding [14], where the failure is initiated by an intralaminar damage associated to σ_{22} intralaminar stresses. For establishing the stress criteria, it is assumed that this intralaminar damage emerges in the 90° ply closest to the inner radius of the curved laminate and that, under sufficiently high σ_{33} interlaminar stresses, this intralaminar damage propagates as a delamination and ultimately leads to the final failure of the laminate. Notice that, with the reference system defined above, σ_{22} intralaminar stresses in the 90° ply are the circumferential stresses directly associated to the applied bending moment. Since the moment tries to open the arms of the sample, it creates tensile σ_{22} stresses in the inner 90° plies with the innermost 90° ply experiencing the highest stresses.

In both UD and non-UD curved laminates, the failure is catastrophic and results in the instantaneous appearance of multiple cracks, making it challenging to predict the specific failure modes accurately.

In the present study, a pointwise strength criterion for the onset of induced unfolding in non-UD laminates is presented, particularly considering in plane and out of plane strengths S_{22} and S_{33}.

To this end, the stress analysis tool presented in [15] is employed here to evaluate the stresses under a certain applied moment M, considering also the residual stresses developed during the manufacturing process. The combined effect of residual and applied stresses is expressed as

$$\sigma_{ij}(M, r) = \sigma_{ij}^{T}(r) + M\sigma_{ij}^{M}(r) \tag{2}$$

where σ_{ij}^{T} denotes the residual stresses and σ_{ij}^{M} represents the stresses corresponding to a unit bending moment.

In the context of pure bending state of the curved beam, where shear stresses are neglected, our focus lies in predicting unfolding failure utilizing the maximum stress criterion within the mid-section of the curved part of the sample.

According to the assumptions made, traditional unfolding occurs when the maximum σ_{33} interlaminar stress reaches the interlaminar tensile strength S_{33}. Therefore, the moment causing traditional unfolding, M_{tu}, can be determined from:

$$M_{tu} = \min_{r}\left[\frac{S_{33} - \sigma_{33}^{T}(r)}{\sigma_{33}^{M}(r)}\right] \quad \text{with} \quad \frac{S_{33} - \sigma_{33}^{T}(r)}{\sigma_{33}^{M}(r)} > 0 \tag{3}$$

The occurrence of the first intralaminar damage is also going to be determined using the maximum stress criterion. According to this criterion, intralaminar failure occurs when the maximum σ_{22} intralaminar normal stress reaches the intralaminar tensile strength S_{22}. Therefore,

Table 4
Average ratio between experimental failure moments and analytical predictions for failure in multidirectional samples made of material M2.

Set	M_{exp}/M_{tu}	M_{exp}/M_{fid}	M_{exp}/M_{iu}
M2.MD.09	0.615 ± 0.028	0.900 ± 0.041	0.900 ± 0.041
M2.MD.16a	0.824 ± 0.062	1.203 ± 0.091	1.203 ± 0.091
M2.MD.16b	0.918 ± 0.026	1.341 ± 0.038	1.341 ± 0.038
M2.MD.28	0.774 ± 0.024	1.087 ± 0.033	1.087 ± 0.033
M2.MD.48a	0.967 ± 0.059	1.007 ± 0.061	1.007 ± 0.061
M2.MD.48b	0.784 ± 0.020	1.009 ± 0.026	0.882 ± 0.023

the moment causing first intralaminar damage, M_{fid}, can be determined from:

$$M_{fid} = \min_{r\in INL}\left[\frac{S_{22} - \sigma_{22}^{T}(r)}{\sigma_{22}^{M}(r)}\right] \quad \text{with} \quad \frac{S_{22} - \sigma_{22}^{T}(r)}{\sigma_{22}^{M}(r)} > 0 \tag{4}$$

where $r \in INL$ denotes that only the innermost block of 90° layers are considered.

Notice that, in the study presented in [14], the values of M_{fid} were in very good agreement with the experimentally determined failure moments. However, as will be detailed later, this is not always the case, since sample failure does not always take place immediately after the first intralaminar damage onset. For the intralaminar damage to propagate unstably as a delamination, a certain level of interlaminar stresses should be reached. This level was quantified in the range between 25% and 35% of S_{33} for material M1 in a preliminary study [22]. In this paper, after the parametric study summarized in Appendix A, we adopt the lower bound of this interval, and generalize it for all materials under study, to define the moment required to achieve an interlaminar stress level that enables the propagation of intralaminar damage as delamination, M_{dp}, which is consequently defined as:

$$M_{dp} = \min_{r\in INL}\left[\frac{0.25S_{33} - \sigma_{33}^{T}(r)}{\sigma_{33}^{M}(r)}\right] \quad \text{with} \quad \frac{0.25S_{33} - \sigma_{33}^{T}(r)}{\sigma_{33}^{M}(r)} > 0 \tag{5}$$

In view of (4) and (5), the induced unfolding failure moment, M_{iu}, that is, the moment that causes failure of the sample after an intralaminar damage propagates unstably as a delamination is defined as:

$$M_{iu} = \max\left[M_{fid}, M_{dp}\right] \tag{6}$$

Based on the previous hypotheses, it is postulated that traditional unfolding occurs when $M_{exp} = M_{tu}$, while induced unfolding takes place when $M_{exp} = M_{iu}$. In the latter case, there are two distinct scenarios. On one hand, if $M_{fid} > M_{dp}$, sample failure is instantaneous after the onset of the first intralaminar damage, while, on the other, if $M_{fid} < M_{dp}$, a certain increase in the applied load is required to cause sample failure after the onset of the first intralaminar damage. Obviously, since failure is catastrophic in all scenarios, in each configuration only the failure mechanism requiring a lower load takes place.

In the following section, a detailed analysis of the stress state in the samples of the test campaign is conducted to demonstrate that the failure mechanism in each case can be predicted with fairly good accuracy using the simple stress-based failure criteria defined above.

4. Failure analysis of material M2 samples

In this section, the studies concerning multidirectional curved laminates made of material M2 available in [14] are revisited to address two key aspects. First, for the lack of information, the assumption that $S_{33} = S_{22}$ was made for material M2 in [14] while distinct experimentally measured values of S_{33} and S_{22} have been employed in the present study. Second, for the sake of simplicity, the effect of residual stresses was approximated in [14], while it has been more rigorously incorporated in the calculations in this study, as described in the previous section. Notwithstanding, the results show that the simplifications made in [14]

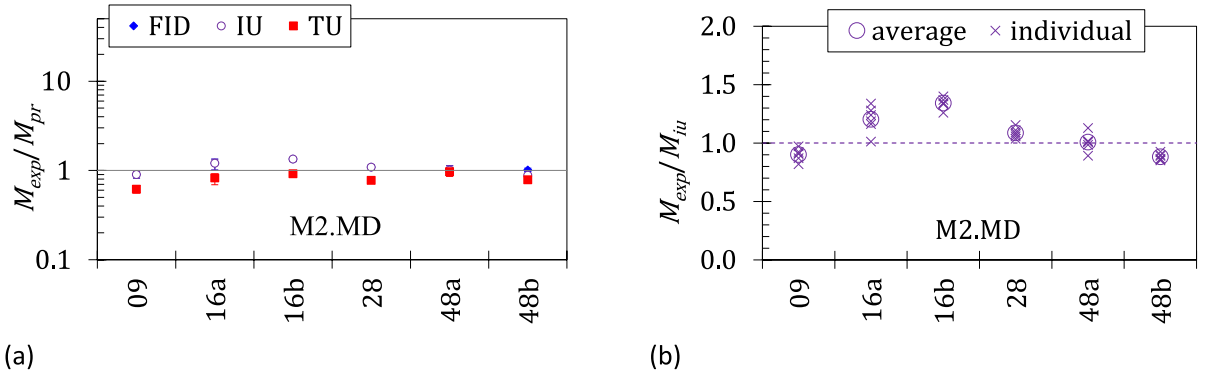

Fig. 4. Ratio between experimental failure moments and analytical predictions in M2.MD samples: (a) all unfolding failure predictions, (b): induced unfolding failure prediction.

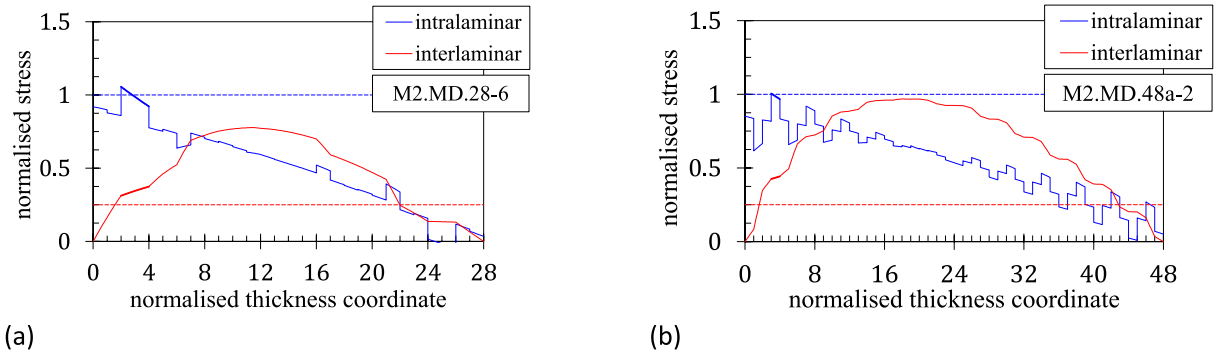

Fig. 5. Evolution of σ_{22}/S_{22} and σ_{33}/S_{33} in typical M2.MD samples at failure: (a) M2.MD.28, (b) M2.MD.48a.

do not significantly affect either the results obtained, or the conclusions derived from them.

Table 4 provides an insightful overview of the ratio of the experimental failure moments, M_{exp}, to the distinct predictions for the failure moment, M_{fid}, M_{iu} and M_{tu}, obtained respectively from (3), (4) and (5), for samples made of material M2. Notably, the comparison of experimental results with predictions for traditional unfolding yields a range of $0.61 \leq M_{exp}/M_{tu} \leq 0.97$. These results provide clear evidence that, when failure occurs, interlaminar stresses are well below the allowable limit. In contrast, the comparison of experimental results with predictions for induced unfolding exhibits a range of $0.90 \leq M_{exp}/M_{iu} \leq 1.34$, suggesting that the occurrence of this failure mechanism is closely aligned with the experimental results. Remarkably, when comparing the values of M_{exp}/M_{fid} with the ratio of experimental results to induced unfolding, M_{exp}/M_{iu} , it can be seen that they are identical in most cases (and very similar when not identical). These results confirm the conclusion drawn in [14], that when the first intralaminar damage takes place, interlaminar stresses are sufficiently high for propagating it as a delamination. Consequently, failure of the sample occurs either instantaneously after the onset of the intralaminar damage or require a slight increase in the applied load.

The ratio of the experimental failure moments to the distinct predictions for the failure moment, M_{exp}/M_{pr}, with $M_{pr} = M_{fid}, M_{iu}, M_{tu}$ (along with the range covered by all individual measurements) are represented in Fig. 4(a), in logarithmic scale. Notice that the scale employed in this plot is the same as the scale employed in Figs. 7(a) and 9(a), where the results for the samples of materials M1 and M3 are presented, to facilitate the comparison between them. For a clearer view

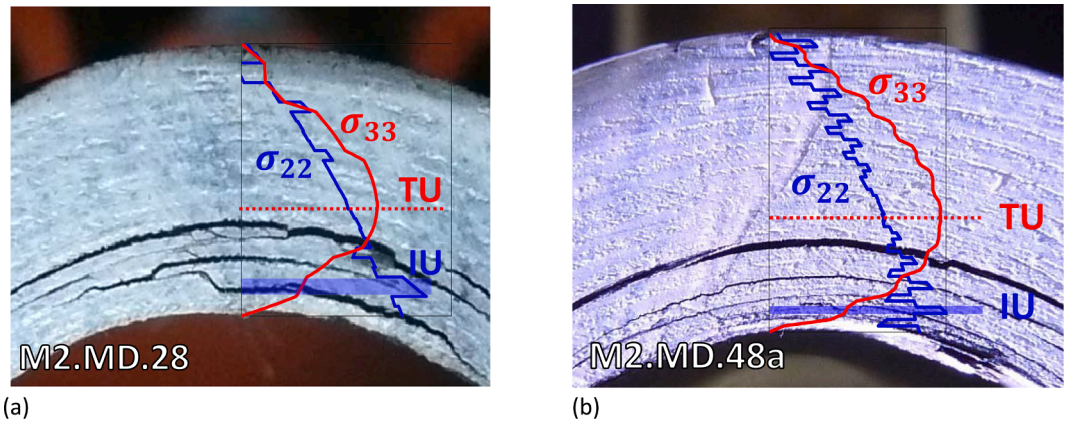

Fig. 6. Correlation between stress solution and failure locations in typical M2.MD samples at failure: (a) M2.MD.28, (b) M2.MD.48a.

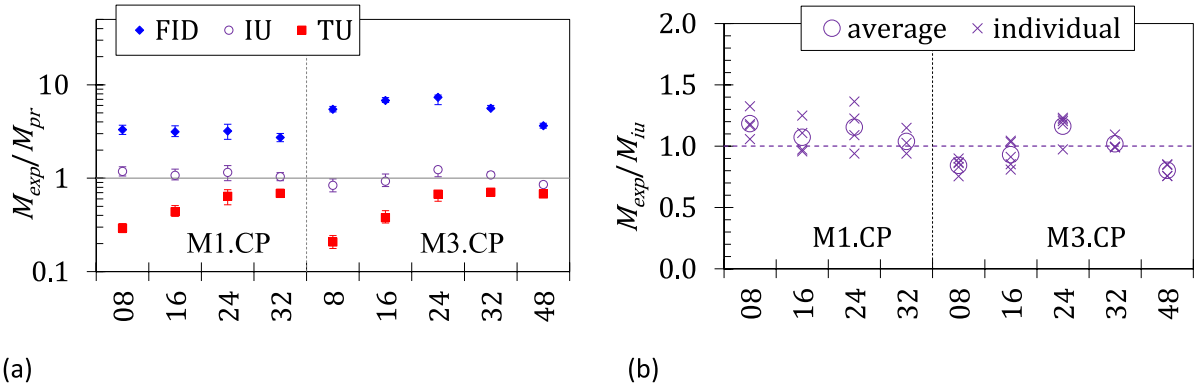

Fig. 7. Ratio between experimental failure moments and analytical predictions in M1.CP and M3.CP samples: (a) all unfolding failure predictions, (b): induced unfolding failure prediction.

of the results of the samples analyzed in this section (for which all predictions are, in fact, relatively close to the experimentally measured failure moment) results of M_{exp}/M_{iu} are presented in Fig. 4(b) in a decimal scale. To show the dispersion of the results, for each set, both the average value and the individual results are presented.

Fig. 5 provides a deeper insight into the failure behavior of the MD samples by showing typical evolutions along the thickness of σ_{22}/S_{22} normalized intralaminar stresses and σ_{33}/S_{33} normalized interlaminar stresses, evaluated using (2) with M being the actual failure moment of each sample. A normalized thickness coordinate ranging from 0 (in the inner part of the sample) to the number of layers is used in the horizontal axis.

Analyzing the stress distributions in both samples, it can be clearly seen that, at the failure moment, σ_{22} reaches its allowable value S_{22} at the innermost 90° ply, i.e. the third ply in the M2.MD.28-6 sample and the fourth ply of the M2.MD.48a-2 sample, thus giving rise to intralaminar damage in these layers. Moreover, within these layers, the interlaminar stresses are sufficiently high to facilitate the propagation of this intralaminar damage as delamination.

As a support of the assumptions made, a critical examination of the damage locations on the broken samples is carried out and compared with the failure predictions to assess the capability of the criterion proposed. Fig. 6 shows two broken samples of the sets M2.MD.28 and M2.MD.48a, overlaid with the solutions for σ_{33} interlaminar stress (in red color) and the σ_{22} intralaminar stress (in blue color). As mentioned above, in both cases, the highest values of σ_{22} are recorded in the innermost 90° layer (marked with shaded blue and the legend IU in the picture) and the images show clear evidence of damage in this region.

Although the failure of the samples is catastrophic and lead to the formation of multiple cracks, all samples present evidence of intralaminar damage in their innermost 90° layer, along with a delamination crack in one of its interfaces. This fact supports the assumptions made in the development of the failure criteria proposed.

5. Failure analysis of material M1 and M3 samples

In this section, the failure of samples made of material M1 and M3 are analyzed following the same procedures described in the previous section.

The ratio of the experimental failure moments to the distinct predictions for the failure moment, M_{exp}/M_{pr}, are represented in Figs. 7(a) and 10(a), where it can be appreciated that the prediction given by M_{iu} is the most accurate in all cases. In the following, the results of these samples are described separately in detail.

Notice that, in contrast to what is obtained for samples of material M2, the load required to induce first intralaminar damage in samples of materials M2 and M3 is significantly lower than the failure load, that is, $M_{exp}/M_{fid} \gg 1$. Notwithstanding, no clear effect on the global stiffness of the specimen can be appreciated in the load/displacement curves (shown in Appendix B).

Table 5
Average ratio between experimental failure moments and analytical predictions for failure in $[0, 90_2, 0_n]_S$ samples.

Set	M_{exp}/M_{tu}	M_{exp}/M_{fid}	M_{exp}/M_{iu}
M1.CP.08	0.292 ± 0.027	3.30 ± 0.30	1.18 ± 0.11
M1.CP.16	0.437 ± 0.055	3.13 ± 0.39	1.07 ± 0.13
M1.CP.24	0.640 ± 0.098	3.20 ± 0.49	1.16 ± 0.18
M1.CP.32	0.689 ± 0.079	2.73 ± 0.31	1.04 ± 0.12
M3.CP.08	0.208 ± 0.012	5.47 ± 0.32	0.844 ± 0.049
M3.CP.16	0.378 ± 0.038	6.79 ± 0.68	0.931 ± 0.093
M3.CP.24	0.640 ± 0.052	7.32 ± 0.59	1.162 ± 0.094
M3.CP.32	0.670 ± 0.033	5.61 ± 0.27	1.019 ± 0.050
M3.CP.48	0.641 ± 0.042	3.64 ± 0.24	0.804 ± 0.052

5.1. Failure analysis of $[0, 90_2, 0_n]_S$ samples

The $[0, 90_2, 0_n]_S$ stacking sequences (CP) employed are detailed in Table 2. Notice that apart from CP1 samples, the rest of the stacking sequences deviate from the general rules of the laminate design. These unconventional stacking sequences were intentionally chosen to incorporate weak layers in the laminates, specifically the 90° layers situated in the inner radii. These weak layers are expected to be the first to experience failure, offering valuable insights into induced unfolding failure mechanism.

Results of CP samples made of materials M1 and M3 are presented in Table 5 and plotted in Fig. 7(a). When comparing the experimental results with predictions for traditional unfolding, we observe a narrow range of $0.2 \leq M_{exp}/M_{tu} \leq 0.69$. This indicates that, at the point of failure, σ_{33} interlaminar stresses are well below the allowable threshold. In contrast, the comparison of experimental results with predictions for first intralaminar damage shows a significantly broader range of $2.73 \leq M_{exp}/M_{fid} \leq 7.32$. In other words, failure occurs at a significantly higher load than that required to create the first intralaminar damage. In contrast with what was observed in the previous section, when the first intralaminar damage takes place, interlaminar stresses are not sufficiently high to propagate this damage as a delamination, thus leading to a considerable discrepancy between the load required to create the onset of intralaminar damage and the actual failure load. Notwithstanding, the comparison of experimental results with predictions for induced unfolding yields a range of $0.80 \leq M_{exp}/M_{iu} \leq 1.18$. These results, visually represented in Fig. 7(b), demonstrate a good alignment between the predicted failure loads and the experimental results, with less than 20% error and underscore the efficiency of the proposed criterion for predicting induced unfolding failure load.

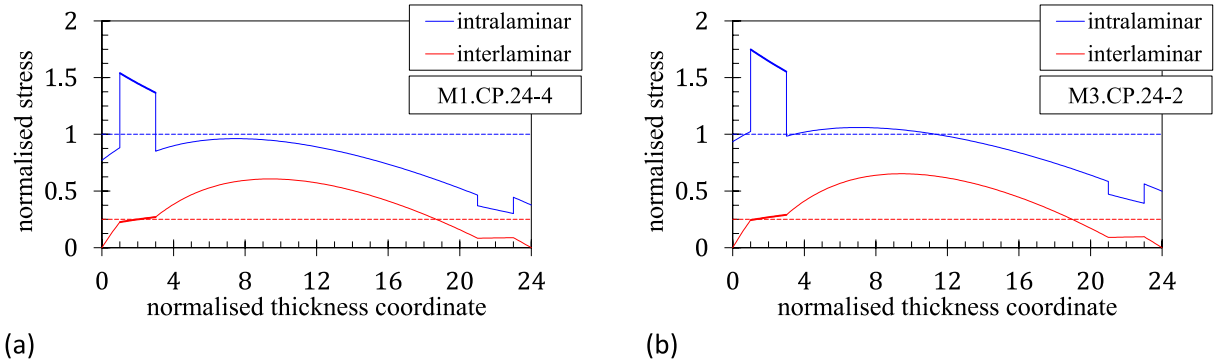

Fig. 8. Evolution of σ_{22}/S_{22} and σ_{33}/S_{33} in typical $[0, 90_2, 0_n]_S$ samples made of materials M1 and M3: (a) M1.CP.24, (b) M3.CP.24.

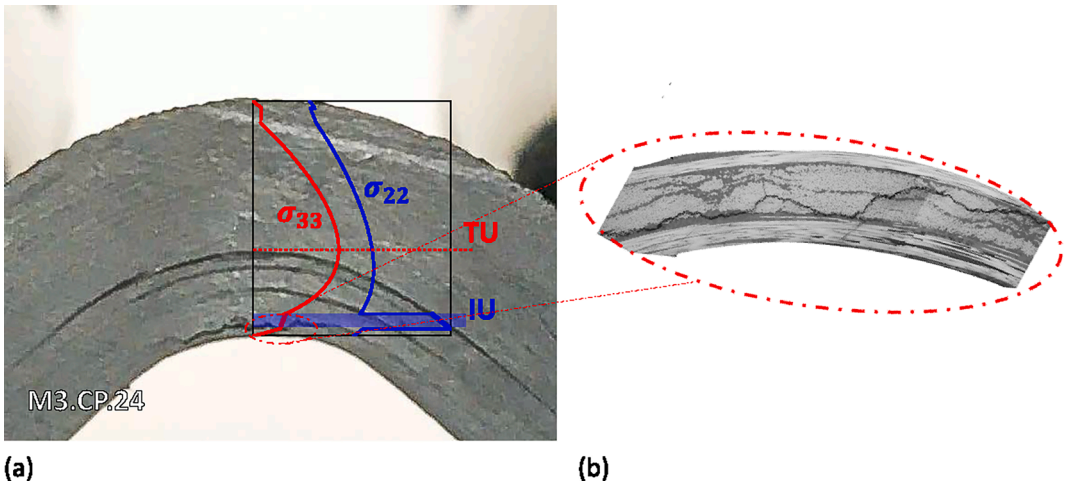

Fig. 9. Correlation between stress solution and failure locations in a typical M3.CP.24 samples: (a) view of the corner; (b) zoom view of the crack in the innermost 90° layer.

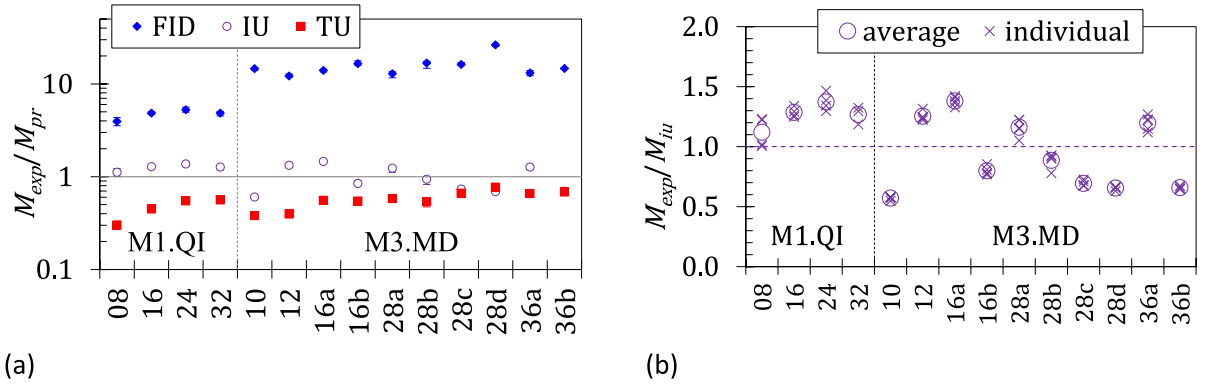

Fig. 10. Ratio between experimental failure moments and analytical predictions in M1.QI and M3.MD samples: (a) all unfolding failure predictions, (b): induced unfolding failure prediction.

Fig. 8 illustrates the σ_{22} and σ_{33} stress distributions in typical 24-ply samples made of materials M1 and M3 calculated analytically using the experimentally measured failure moment. As expected, both plots display a similar pattern (the slight differences arise from the distinct thermal and stiffness properties of the materials), where the σ_{22} intralaminar stresses reach their maximum values in the innermost 90° layer. Within these layers, σ_{22} is clearly above its allowable value, $\sigma_{22}/S_{22} > 1$, that is, significant intralaminar damage should exist in these layers prior to the final failure of the samples. Moreover, the σ_{33} interlaminar stresses in these layers are observed to be reasonably equal to the limit considered for the intralaminar damage to propagate as a delamination, $\sigma_{33}/S_{33} = 0.25$. Although not shown here for the lack of space, this consistent trend is observed across all the CP samples.

Fig. 9 displays the stress distributions superimposed on the tested M3.CP.24-2 sample, providing clear visualization of the correspondence between the predicted location for failure initiation and one of the actual crack locations within the laminate, further supporting the suitability of the proposed approach for predicting the unfolding failure mechanisms. Fig. 9(b) provides a microscopic image of the section of inner block of 90° plies, where the intralaminar crack can be seen propagating from the

Table 6
Average ratio between experimental failure moments and analytical predictions for failure in multidirectional samples made of materials M1 and M3.

Set	M_{exp}/M_{tu}	M_{exp}/M_{fid}	M_{exp}/M_{iu}
M1.QI.08	0.302 ± 0.033	3.94 ± 0.43	1.12 ± 0.12
M1.QI.16	0.448 ± 0.014	4.83 ± 0.15	1.285 ± 0.040
M1.QI.24	0.549 ± 0.028	5.25 ± 0.27	1.372 ± 0.070
M1.QI.32	0.561 ± 0.037	4.84 ± 0.32	1.267 ± 0.083
M3.MD.10	0.3616 ± 0.0077	14.59 ± 0.31	0.571 ± 0.012
M3.MD.12	0.3743 ± 0.0095	12.19 ± 0.31	1.253 ± 0.032
M3.MD.16a	0.527 ± 0.012	13.97 ± 0.33	1.380 ± 0.033
M3.MD.16b	0.518 ± 0.020	16.56 ± 0.64	0.797 ± 0.031
M3.MD.28a	0.550 ± 0.029	12.88 ± 0.69	1.160 ± 0.062
M3.MD.28b	0.509 ± 0.031	17.0 ± 1.0	0.886 ± 0.053
M3.MD.28c	0.630 ± 0.019	16.23 ± 0.50	0.693 ± 0.021
M3.MD.28d	0.730 ± 0.014	26.33 ± 0.49	0.654 ± 0.012
M3.MD.36a	0.623 ± 0.028	13.13 ± 0.59	1.196 ± 0.054
M3.MD.36b	0.647 ± 0.011	14.70 ± 0.24	0.657 ± 0.011

lower 90° layer to the upper 90° layer.

5.2. Failure analysis of quasi-isotropic and multidirectional samples

The stacking sequences of the quasi-isotropic (QI) laminates made of material M1 and multidirectional (MD) laminates made of material M3 are provided in Table 2. It is important to highlight that for QI laminates, stacking sequences were deliberately selected to achieve a low M_{fid}/M_{tu} ratio, indicating that the failure initiation is expected to occur in the innermost 90° layers prior to interlaminar failure. Conversely, the MD laminates were designed with typical layups commonly employed in the corners of actual composite structures, making it more representative of practical applications in the aeronautical industry.

Table 6 and Fig. 10(a) provide a comprehensive comparison of the experimental results with the predictions for both QI and MD samples. When examining the experimental results in comparison to the predictions for traditional unfolding, a range of $0.30 \leq M_{exp}/M_{tu} \leq 0.73$ is observed. These results reaffirm the findings seen in $[0, 90_2, 0_n]_S$ samples, indicating that at the point of failure, the interlaminar stresses are far below their allowable value. Conversely, when considering the experimental results in relation to the predictions for first intralaminar damage, a significantly broader range of $3.94 \leq M_{exp}/M_{fid} \leq 26.33$ is observed. This substantial difference between the onset of first intralaminar damage and the actual failure signifies that a very high increase in the applied load is required in some cases to cause the failure of the sample after experiencing the first intralaminar damage. Remarkably, when comparing the experimental results with predictions for induced unfolding, shown in Fig. 10(b), a significantly good agreement is observed, with a range of $0.57 \leq M_{exp}/M_{iu} \leq 1.38$.

Furthermore, Fig. 11 presents typical stress distributions in M1.QI.32-1 and M3.MD.16b-3 samples. As observed in the previous cases, both QI and MD laminates exhibit maximum intralaminar stresses in the innermost 90° layers in both QI and MD samples. Notice that, in these layers, σ_{22} is well above its allowable value, $\sigma_{22}/S_{22} > 1$, and, therefore, significant intralaminar damage should exist in these layers prior to the final failure of the samples. Moreover, supporting the assumption made for the propagation of the intralaminar damage as a delamination, it can be clearly appreciated that the σ_{33} interlaminar stresses in 90° are reasonably equal to the limit considered, that is, $\sigma_{33}/S_{33} = 0.25$.

Fig. 12 displays the stress distributions superimposed onto a typical sample of the M3.MD.28a and M3.MD.36a sets, where it can be clearly observed the wavy intralaminar damage in the innermost block of 90°

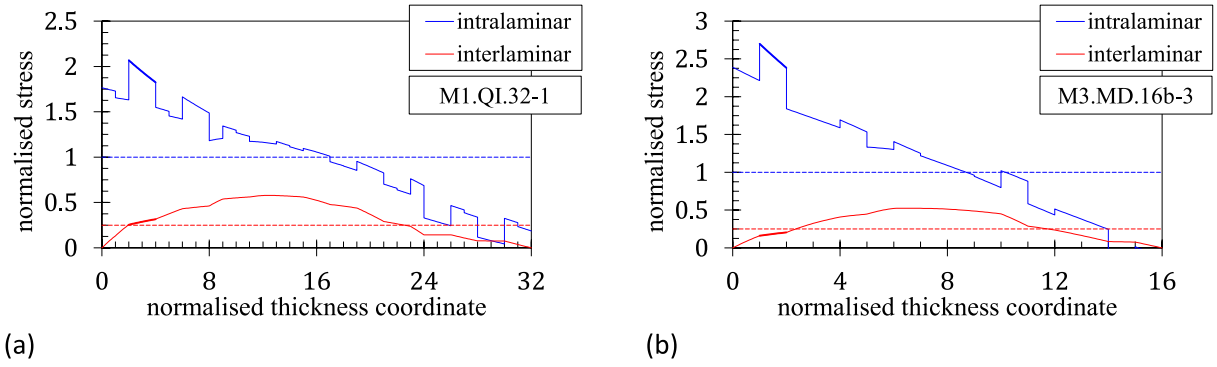

Fig. 11. Evolution of σ_{22}/S_{22} and σ_{33}/S_{33} in typical multidirectional samples at failure: (a) M1.QI.32, (b) M3.MD.16b.

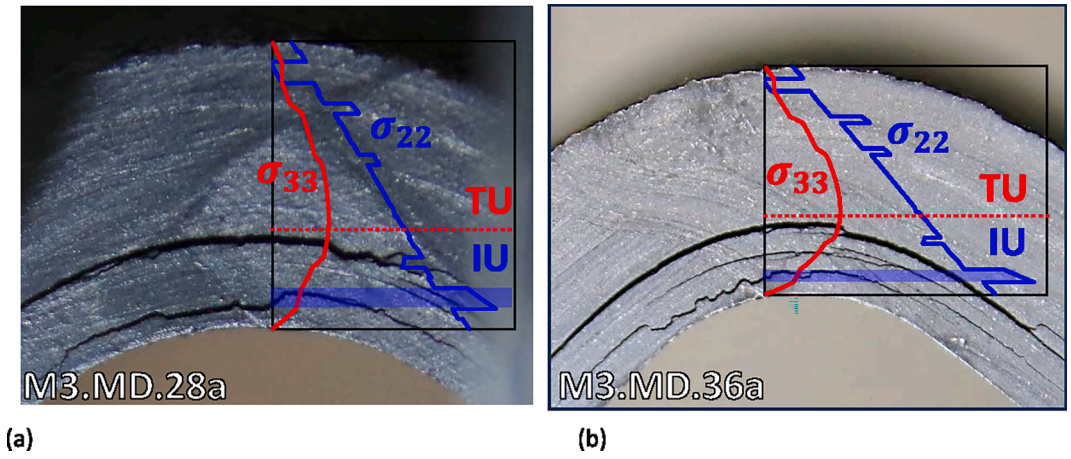

Fig. 12. Correlation between stress solution and failure locations in typical multidirectional samples at failure: (a) M3.MD.28a, (b) M3.MD.36a.

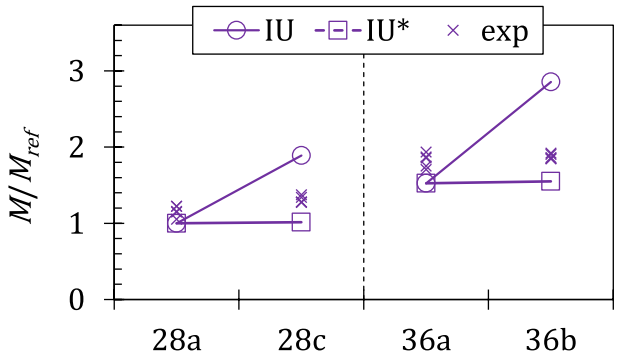

Fig. 13. Effect of separating the innermost block of 90° layers. M represents each experimental or predicted failure moment and M_{ref} is the IU failure moment prediction of the M3.MD.28a set.

layers and the delamination crack arising from it.

6. Discussion

The coherent agreement between the predicted and actual failure loads and locations undoubtedly support the assumptions in which the proposed criterion for predicting failure modes in composite laminates is based. However, there are some instances where certain deviations from the predicted outcomes can be observed. In subsequent subsections, we examine these discrepancies and explore potential causes that might contribute to the observed deviations.

With the analysis tool developed, regularized stresses in the interior of the curved region are employed to obtain the failure predictions. Consequently, the effect of the free-edge stresses is not considered here (see [24] and references therein). Up to a 16 % increase in the *CBS* was reported in [25] when free-edge effect is reduced using a resin edge treatment. Free-edge effects may be an alternative potential cause contributing to the observed deviations. Notwithstanding, notice that, w/t ratios higher than those defined by ASTM standard [20] have been employed, which reduces the effect of the free-edge stresses.

6.1. Separation of the 90° layers

When comparing pairs M3.MD.28a/M3.MD.28c and M3.MD.36a/M3.MD.36b, the first set has a stacking sequence featuring a block of two 90° layers together $[45, -45, 90_2, \cdots]_S$ while in the second set, the block is distributed in the form $[45, 90, -45, 90, \cdots]_S$. As depicted in Fig. 13, separating the 90° layers does not significantly affect the failure load.

Notice that, in the samples with separated 90° layers, the failure prediction is notably improved if we consider that failure initiates in the second 90° layer (IU*) instead of the innermost 90° layer.

Stress analysis reveals that in samples with separated 90° layers, σ_{33} stresses in the innermost 90° are below their limit value, while stresses in the second 90° layer are at the limit, as can be seen in Fig. 14. Post-failure images confirm that failure might have initiated in the second 90° layer, as evident in the comparison between Fig. 15 with Fig. 12.

However, it's important to note that this pattern is not consistently observed in all stacking sequences. For instance, in Fig. 11, the sample M1.Q1.32 features two blocks of two 90° layers, and failure seems to be triggered in the innermost, despite the induced unfolding failure criteria being fulfilled at a lower load in the second block.

Notice that, although a thickness dependence of S_{22} has been re-

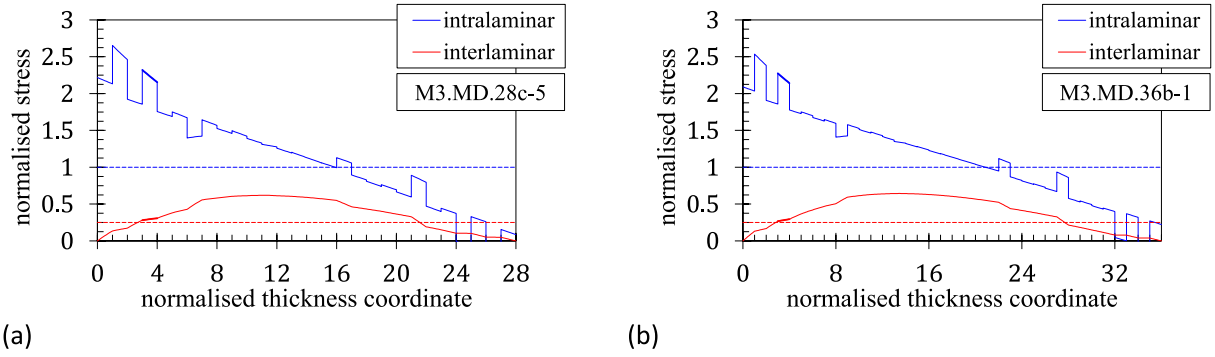

Fig. 14. Evolution of σ_{22}/S_{22} and σ_{33}/S_{33} in typical multidirectional samples at failure: (a) M3.MD.28c, (b) M3.MD.36b.

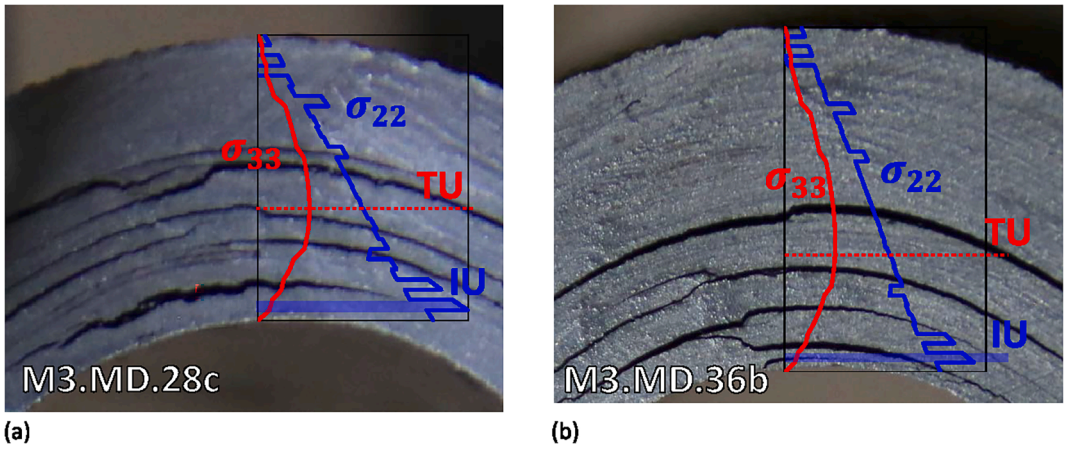

Fig. 15. Correlation between stress solution and failure locations in typical multidirectional samples at failure: (a) M3.MD.28c, (b) M3.MD.36b.

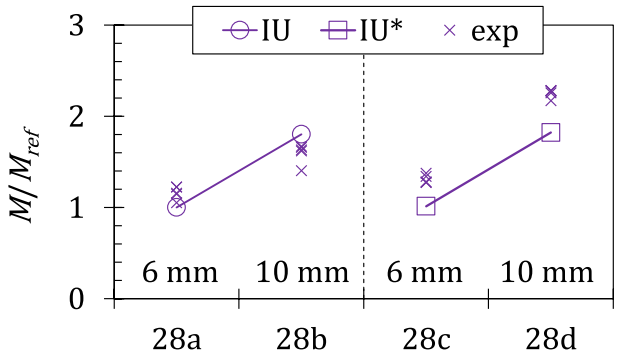

Fig. 16. Effect of separating the innermost block of 90° layers. M represents each experimental or predicted failure moment and M_{ref} is the IU failure moment prediction of the M3.MD.28a set.

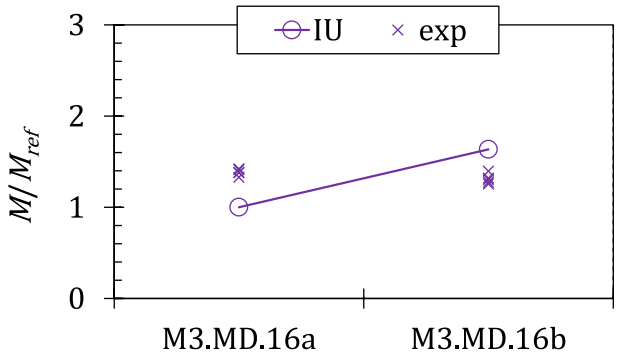

Fig. 17. Effect of moving outwards the 90° layer. M represents each experimental or predicted failure moment and M_{ref} is the IU failure moment prediction of the M3.MD.16a set.

ported in [26,27] for flat laminates, the same value has been considered here in all cases since transverse stresses are linearly varying in the block of 90° layers and transverse damage is assumed to appear mostly in the region close to its inner interface, where the transverse stresses are higher.

6.2. Increasing the inner radius

To show the significant effect of the inner radius of the corner on its failure load, pairs M3.MD.28a/M3.MD.28b and M3.MD.28c/M3.MD.28d have been designed in a way that, in each pair, the first set has $r_i = 6$ mm and the second $r_i = 10$ mm, while keeping the same stacking sequence.

As depicted in Fig. 16, experimental results clearly demonstrate that increasing r_i significantly increases the load that the corner can sustain. Notice that the proposed failure criteria can predict accurately this increase, provided the correct 90° layer in which failure initiated is identified.

6.3. Effect of moving 90° layer outwards

Comparing pairs M3.MD.16a/M3.MD.16b which only differ in the position of the innermost 90° layer, experimental results show that both sets can sustain the same load, see Fig. 17.

According to predictions, relocating the 90° layer outwards, would increase the failure load (since interlaminar stresses, displayed in Fig. 18, are lower in the 90° layer). Notwithstanding, predictions are not accurate in these samples (a possible reason for that being that they are very thin and thus more affected by fiber wrinkling) and a more detailed analysis is required.

7. Concluding remarks

In this paper, we conducted an extensive experimental test campaign using three different thermoset materials and distinct stacking sequences to investigate the failure in curved composite laminates. Our primary objective was to assess the induced unfolding failure phenomenon in non-UD laminates by utilizing a simple pointwise stress criterion to determine the induced unfolding failure moment M_{iu}.

The comparison between experimental results and predictions demonstrated consistent agreement for experimentally measured failure moments and M_{iu} failure moment predictions.

In all cases, failure occurs below the load needed to cause pure interlaminar failure, M_{tu}, thus supporting the hypothesis that, in most cases, unfolding failure is initiated by an intralaminar damage.

For material M2, in which $S_{22} > S_{33}$, the load required to induce first intralaminar damage, M_{fid}, in all sets considered is very similar or equal to M_{iu}, meaning that failure of the sample is instantaneous after intralaminar damage. For materials M1 and M3, where $S_{22} < S_{33}$ in all sets considered $M_{fid} < M_{iu}$, therefore, an increase in the applied load is required to cause the first intralaminar damage to propagate as subsequent delamination.

The majority of the sets analysed exhibited coherent agreement when comparing the test results with the induced unfolding failure predictions. Moreover, stress analysis and assumed damage initiation locations also agree with the location of the cracks in the failed samples.

Some specimens showed certain deviations from the predicted results, shedding light on the limitations of the proposed criterion. Notwithstanding, a high dispersion of the results is inherent to the failure of highly curved laminates and, despite the simplicity of the criterion proposed, the overall agreement in predicting the induced unfolding failure load in multidirectional stacking sequences is similar to the agreement obtained in predicting the traditional unfolding load in

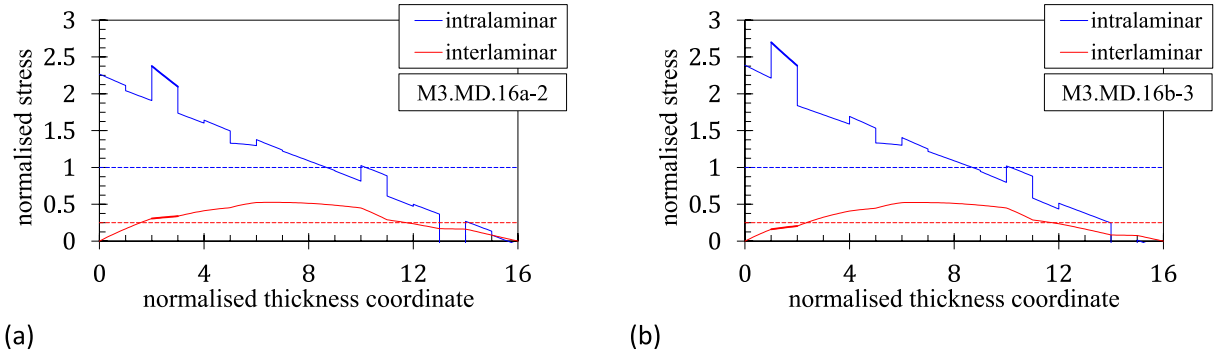

Fig. 18. Evolution of σ_{22}/S_{22} and σ_{33}/S_{33} in typical multidirectional samples at failure: (a) M3.MD.16a, (b) M3.MD.16b.

UD-laminates.

CRediT authorship contribution statement

S. Bushpalli: Writing – review & editing, Writing – original draft, Visualization, Validation, Methodology, Investigation, Formal analysis, Data curation. **P. Zumaquero:** Methodology, Formal analysis, Data curation, Investigation, Validation, Visualization. **B. López-Romano:** Writing – review & editing, Supervision, Resources, Project administration, Funding acquisition. **E. Graciani:** Writing – review & editing, Visualization, Validation, Supervision, Resources, Methodology, Investigation, Funding acquisition, Data curation, Conceptualization.

Declaration of competing interest

The authors declare that they have no known competing financial interests or personal relationships that could have appeared to influence the work reported in this paper.

Data availability

Data will be made available on request.

Acknowledgements

The authors gratefully acknowledge Airbus Operations S.L. and TEAMS S.L. for their support and the input of the experimental results. This work has been funded by the Ministerio de Economía y Competitividad of Spain (Project: MAT2015-71309-P, MINECO/FEDER) and by the European Commission (Marie Skłodowska-Curie Actions, Grant Agreement n° 861061, Project: NEWFRAC).

Appendix A. Pointwise stress criterion for induced unfolding

The induced unfolding failure criteria used in this work is based on the assumption that unfolding failure is initiated in the innermost block of 90° plies, where intralaminar stresses $\sigma_{22} > S_{22}$ create an intralaminar damage which in the presence of sufficiently high interlaminar stresses $\sigma_{33} > kS_{33}$ (with $k = 0.25$) causes an intralaminar crack that further propagates as a delamination.

Notice that, although this failure mechanism resembles the failure mechanism of a $[0, 90_n, 0]$ flat laminate loaded in tension, there are significant differences. In flat laminates, transverse stresses in the 90° plies are constant, and once the transverse strength S_{22} is reached transverse cracks appear spanning almost the whole width of the block of 90° plies. A sufficient increase in the applied load results in the appearance of delamination cracks at the interfaces between the 0° and 90° plies, which start from the tip of the transverse cracks.

Crack paths seen in the innermost block of 90° plies of the unfolding samples show a significantly different pattern, see for instance Figs. 9 and 12. Instead of a set of transverse cracks with interfacial delamination cracks arising from them, a single (sometimes branched) longitudinal interlaminar crack with an intricate path is seen in the curved region, which eventually migrates to the interfaces of the block of 90° plies and propagates into the straight arms as delamination.

Since the sample is loaded in bending, transverse stresses are linearly decreasing from the inner to the outer interfaces of the innermost block of 90° plies. Consequently, when the transverse strength S_{22} is reached, a certain damage is created in these plies (without forming a transverse crack). This intralaminar damage weakens the plies until a sufficiently high interlaminar stress causes the appearance of a longitudinal crack which grows unstably causing a significant loss of stiffness and sample failure.

Preliminary analysis carried out by the authors and coworkers, using fracture mechanics approaches capable of modelling damage onset and propagation, like finite fracture mechanics and phase-field modeling of fracture, confirm the feasibility of the abovementioned failure mechanism. Notwithstanding, for design purposes, a simple empirical stress-based failure criteria, like the one presented in this paper, is of great practical interest.

In Fig. 19, the results of a sensitivity analysis of the proposed stress-based criteria for unfolding failure, which combines $\sigma_{22} > S_{22}$ and $\sigma_{33} > kS_{33}$ is presented. The induced unfolding failure moment $M_{iu}(k)$ is determined following (4)-(6), replacing the 0.25 reduction coefficient in (5) by a parameter k. To include all non-UD samples considered in this study, results are non-dimensional, dividing, for each sample configuration, the induced unfolding failure moment by the average experimental *CBS* of the individual samples, M_{av}.

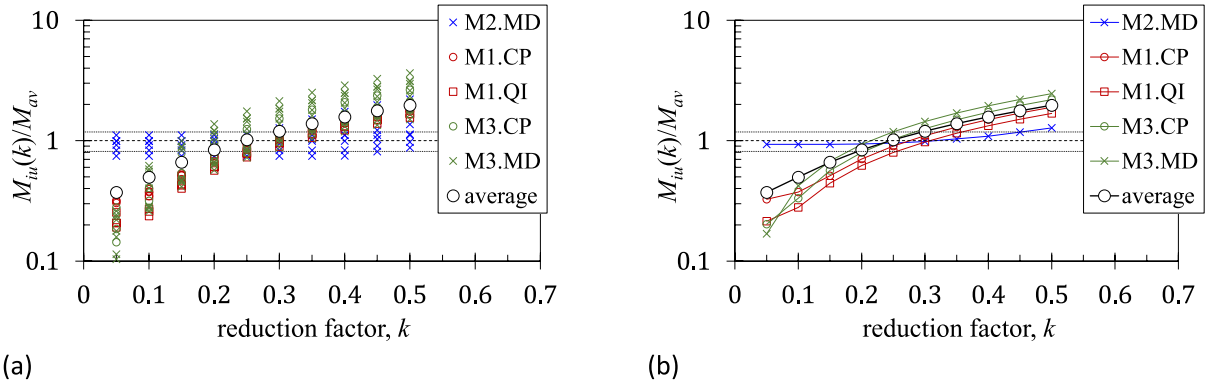

Fig. 19. Induced unfolding failure criteria sensitivity analysis: (a) all configurations, (b) set averages.

In Fig. 19(a) and (b) the black dots represent the average of all configurations. As can be seen, the best agreement between analytical predictions and experimental results $M_{iu}(k)/M_{av} = 1$ is obtained when $k \cong 0.25$. To gain an insight into the dispersion of the results all configurations analyzed are represented with different colors in Fig. 19(a), where it can be seen that the lower dispersion is also obtained when $k \cong 0.25$. For the sake of comparison, doted lines indicate the lower and upper bounds of the ratio between the individual and averaged experimental *CBS* measurements. To better distinguish the results corresponding to the different sets of samples considered, results of all configurations in each set are represented averaged in Fig. 19(b).

Appendix B. Experimental plots of M1 and M3 samples

Experimental load/displacement response of multidirectional samples of material M1 and M3 are respectively shown in Figs. 20 and 21. For confidentiality reasons scale in Fig. 21 is undisclosed.

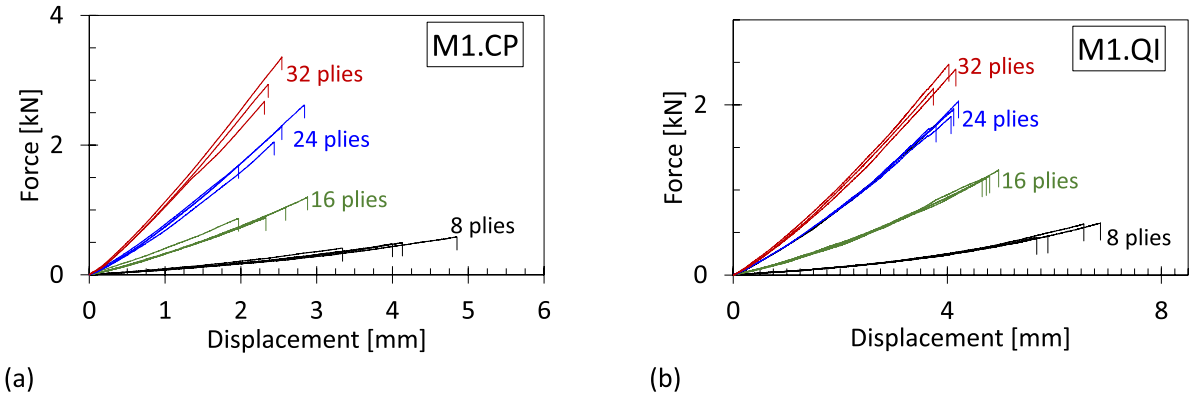

Fig. 20. Experimental load/displacement plots of: (a) M1.CP samples, (b) M1.QI samples.

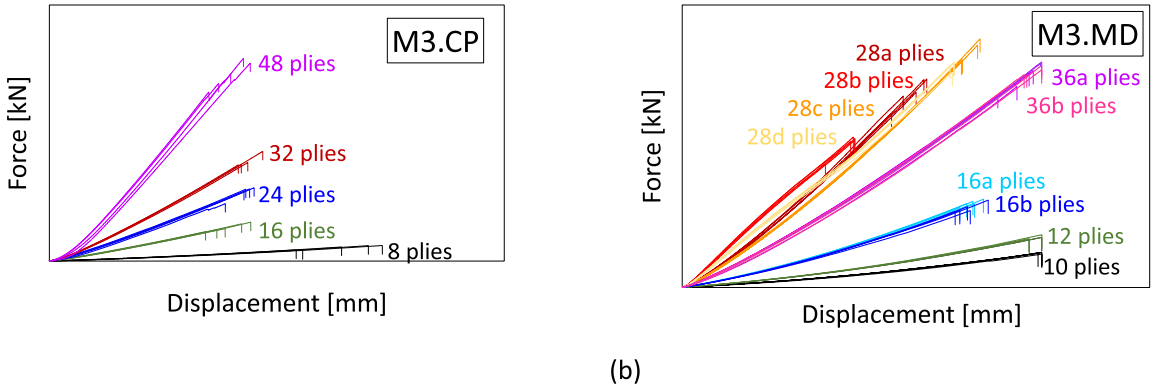

Fig. 21. Experimental load/displacement plots of: (a) M3.CP samples, (b) M3.M3 samples.

References

[1] Sun CT, Kelly SR. Failure Analysis of Composite Angle Structures. In: Developments in the Science and Technology of Composite Materials. In: Proc. of the First European Conference on Composite Materials and Exhibition. Bordeaux, France 1985 (pp. 277-284).

[2] Sun CT, Kelly SR. Failure in composite angle structures Part II: onset of delamination. J Reinf Plast Compos 1988;7(3):233–44.

[3] Martin RH, Jackson WC. Damage prediction in cross-plied curved composite laminates. Compos Mater: Fatigue Fract 1993;4:105–26.

[4] Hélénon F, Wisnom MR, Hallett SR, Trask RS. Numerical investigation into failure of laminated composite T-piece specimens under tensile loading. Compos A Appl Sci Manuf 2012;43(7):1017–27.

[5] Roos R, Kress G, Ermanni P. A post-processing method for interlaminar normal stresses in doubly curved laminates. Compos Struct 2007;1;81(3):463–70.

[6] Kim R, Soni S. Failure of composite laminates due to combined interlaminar normal and shear stresses. Proc Japan-US CCM-III 1986:341–50.

[7] Brewer JC, Lagace PA. Quadratic stress criterion for initiation of delamination. J Compos Mater 1984;22:1141–55. https://doi.org/10.1177/002199838802201205.

[8] Edwards T, Thompson J. Spar corner radius integrity for the A400M wing. Appl Mech Mater 2005;3–4:197–204. https://doi.org/10.4028/www.scientific.net/amm.3-4.197.

[9] Huchette C, Vandellos T, Laurin F. Influence of intralaminar damage on the delamination crack evolution. Damage Growth Aerospace Compos 2015:107–40.

[10] Charrier JS, Laurin F, Carrère N, Mahdi S. Determination of the out-of-plane tensile strength using four-point bending tests on laminated L-angle specimens with different stacking sequences and total thicknesses. Compos Part A Appl Sci Manuf 2016;81:243–53. https://doi.org/10.1016/j.compositesa.2015.11.018.

[11] Michel L, Garcia S, Yao C, Espinosa C, Lachaud F. Experimental and numerical investigation of delamination in curved-beam multidirectional laminated composite specimen. Key Eng Mater 2015;577:389–92.

[12] Hoffmann M, Zimmermann K, Bautz B, Middendorf P. Size effect on through thickness strength properties of 3D loaded composite laminates, 2016. ECCM-17, Munich, Germany.

[13] Journoud P, Bouvet C, Castanié B, Laurin F, Ratsifandrihana L. Experimental and numerical analysis of unfolding failure of L-shaped CFRP specimens. Compos Struct 2020;232:111563.

[14] González-Cantero JM, Graciani E, López-Romano B, París F. Competing mechanisms in the unfolding failure in composite laminates. Compos Sci Technol 2018;156:223–30.

[15] González-Cantero JM. Study of the unfolding failure of curved composite laminates. University of Seville; 2017. PhD Thesis.

[16] Spencer AJM, Watson P, Rogers TG. Mathematical analysis of the springback effect in laminated thermoplastic channel sections. Compos Manuf 1991;2:253–8.

[17] National Institute for Aviation Research. Hexcel 8552 AS4 Unidirectional Prepreg at 190 gsm & 35% RC, Qualification Material Property Data Report. Revision A. CAM-RP-2010-002 2011.

[18] Graciani E, Justo J, Zumaquero PL. Determination of in-plane and through-the-thickness coefficients of thermal expansion in composite angle brackets using digital image correlation. Compos Struct 2020;238:111939.

[19] Airbus. Determination of Curved-Beam Failure Load. Issue 2. AITM1-0069 2011.

[20] ASTM International. Standard test method for measuring the curved beam strength of a fiber-reinforced Polymer-matrix composite. ASTM D6415/D6415M-06a 2012.

[21] Zumaquero PL, Justo J, Graciani E. On the thickness dependence of ILTS in curved composite laminates. Key Eng Mater 2018;774:523–8.

[22] Zumaquero PL, Graciani E, Justo J. Fallo por unfolding en laminados curvos de material compuesto: campaña de ensayos y análisis tensional. Anales de Mecánica de la Fractura 2019;36:273–8.

[23] Taylor JR. An introduction to error analysis. The study of uncertainties in physical measurements, second ed., University Science Books, Sausalito, 1997.

[24] Mittelstedt C, Becker W, Kappel A, Kharghani N. Free-edge effects in composite laminates-a review of recent developments 2005–2020. Appl Mech Rev 2022;74:010801.

[25] Fletcher TA, Kim T, Dodwell TJ, Butler R, Scheichl R, Newley R. Resin treatment of free edges to aid certification of through thickness laminate strength. Compos Struct 2016;146:26–33.
[26] Dvorak GJ, Laws N. Analysis of progressive matrix Cracking in composite laminates II. first ply failure. J Compos Mater 1987;21:309–29.
[27] Camanho PP, Dávila CG, Pinho ST, Iannucci L, Robinson P. Prediction of in situ strengths and matrix cracking in composites under transverse tension and in-plane shear. Compos A Appl Sci Manuf 2006;37:165–76.